CHAPTER 12

QuantImage: An Online Tool for High-Throughput 3D Radiomics Feature Extraction in PET-CT

Yashin Dicente Cid[,a,*,**], Joël Castelli[†,‡,§], Roger Schaer[*], Nathaniel Scher[†], Anastasia Pomoni[¶], John O. Prior[¶] and Adrien Depeursinge[*,‖]

* University of Applied Science Western Switzerland (HES-SO), Institute of Information Systems, Sierre, Switzerland.
** University of Geneva, Computer Vision and Multimedia Laboratory, Geneva, Switzerland.
† Lausanne University Hospital (CHUV), Radiotherapy Department, Lausanne, Switzerland.
‡ INSERM, U1099, Rennes, F-35000, France.
‡ Université de Rennes 1, LTSI, Rennes, F-35000, France.
¶ Lausanne University Hospital (CHUV), Nuclear Medicine and Molecular Imaging Department, Lausanne, Switzerland.
‖ École Polytechnique Fédérale de Lausanne (EPFL), Biomedical Imaging Group, Lausanne, Switzerland.
[a] Corresponding: yashin.dicente@hevs.ch

Contents

Abstract

The processes of radiomics consist of image-based personalized tumor phenotyping for precision medicine. They complement slow, costly and invasive molecular analysis of tumoral tissue. Whereas the relevance of a large variety of quantitative imaging biomarkers has been demonstrated for various cancer types, most studies were based on 2D image analysis of relatively small patient cohorts. In this work, we propose an online tool for automatically extracting 3D state-of-the-art quantitative imaging features from large batches of patients. The developed platform is called QuantImage and can be accessed from any web browser. Its use is straightforward and can be further parameterized for refined analyses. It relies on a robust 3D processing pipeline allowing normalization across patients and imaging protocols.

The user can simply drag-and-drop a large zip file containing all image data for a batch of patients and the platform returns a spreadsheet with the set of quantitative features extracted for each patient. It is expected to enable high-throughput reproducible research and the validation of radiomics imaging parameters to shape the future of non-invasive personalized medicine.

Keywords: Quantitative imaging biomarkers, radiomics, texture analysis, medical imaging, radiology, web technologies, precision medicine.

1. Introduction

Cancer ecosystems are composed of micro-habitats defining the cancer subtype, stage, response to treatment, and patient survival [28]. Estimating the composition of tumoral tissue can therefore provide valuable information for optimal personalized disease management. Current promising approaches for precision medicine are mostly based on molecular analyses of biopsied or resected tissue [47]. Nevertheless, the success of such approaches are hindered by their invasiveness as well as the requirement of slow, costly and complex analysis of "-omics" data. In addition, the tissue samples used for molecular analyses are most often acquired from a highly localized tumor region or from the grinding of whole tumor mass, which does not allow to accurately capture molecular heterogeneity [30]. The computerized quantitative analysis of existing diagnostic, treatment planning and follow-up images enables reproducible and comprehensive analysis of tumoral regions as a whole, potentially allowing the exploration of tumor heterogeneity in a non-invasive fashion. The latter spawned the new research fields of *radiomics* [40] and *imaging genomics* [36] (see Chapter 8). The metabolism, density and structure of tumoral tissue observed in three-dimensional Positron Emission Tomography (PET), Magnetic Resonance (MR) and Computed Tomography (CT) images reflects their nature [41], including regions of active cancer cells, angiogenesis, necrosis [1] and even subsets of underlying cancer-related genomics [32, 31]. Examples of PET and CT images of heterogeneous Non-Small Cell Lung Cancer (NSCLC) tumors are depicted in Fig. 12.1.

Radiomics consists of image-based personalized tumor phenotyping, complementing slow, costly and invasive molecular analysis [40, 48]. Computerized quantitative image analysis yields a collection of variables, which are further linked to disease outcomes and sub-types using advanced statistical and machine learning methods. These processes are detailed in Fig. 12.2. The main categories of quantitative imaging biomarkers are intensity, shape and texture, which are characterizing the distribution of voxel values, the contour of tumors and the spatial transitions between

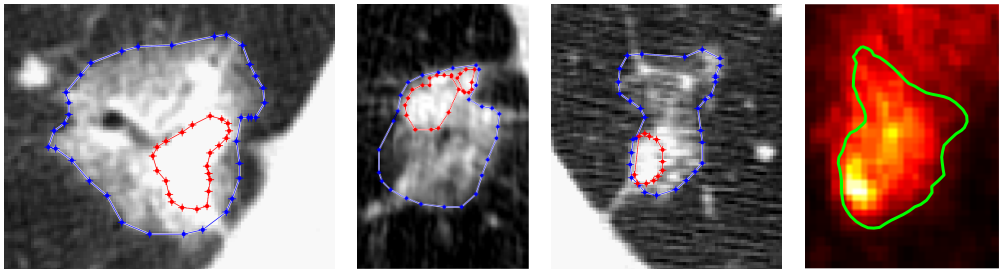

Figure 12.1: Axial views of heterogeneous NSCLC tumors. The three CT images on the left show tumors with solid (red) and ground glass (blue) regions delineated. The PET image on the right shows the metabolic heterogeneity of the tumor.

voxel values, respectively. Current state-of-the-art in radiomics provided initial evidence about the relevance of these quantitative imaging parameters for precision medicine [26, 52, 44, 19, 8]. However, several limitations are concerning texture-based image measures in particular. First, large-scale clinical studies are required to further validate texture-based features in diverse disease-specific contexts. This is of primary importance because texture parameters are mostly informative when used in large groups (*e.g.*, 50 to 100 attributes), requiring large cohorts of patients to respect acceptable ratios between the number of variables and instances. Second, most studies are based on sub-optimal texture operators applied in 2D slices that are not able to capture the wealth of complex three-dimensional tissue architectures available in modern imaging protocols (see Chapter 3). 3D approaches are emerging [16]. However, the interpretation of such image measures is challenging since the human cannot fully visualize opaque 3D solid images. Moreover, few computer tools are available and they are not specific to PET and CT imaging. Exceptions include LifeX[28] and CGITA[29] [21], which allow extracting three-dimensional texture measures. However, they are both based on gray-level matrices only, which have shown limited abilities to mine rich textural patterns (see Section 3 of Chapter 3).

This work presents an online tool for extracting high-throughput, advanced 3D radiomics features in PET-CT images. No software installation is required and the platform can be accessed through any web browser. It allows submitting large batches of patient files and to download resulting patient-wise collections of radiomics features in a standard Comma-Separated Values (CSV) data structure. The radiomics attributes include PET- and CT-specific intensity values, novel distance measures characterizing metastatic spread, as well as three distinct groups of texture measurements combining

[28] `http://www.lifexsoft.org`, as of 5 December 2016.
[29] `https://code.google.com/archive/p/cgita/`, as of 5 December 2016.

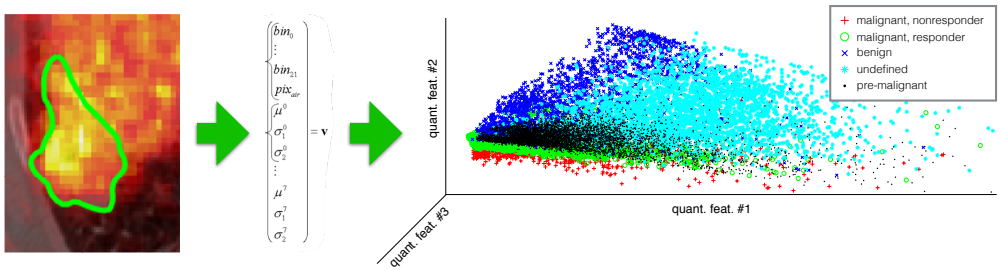

Figure 12.2: Illustration of the radiomics processes (toy example): Several quantitative imaging features are extracted from the tumoral region (green) in PET-CT. The resulting collection of variables spans a hyperspace where distinct cancer sub-types and treatment responders are ideally occupying well-defined regions. The latter can be further revealed by advanced statistical and machine learning methods.

advanced analysis and interpretability. All attributes can be parameterized in a simple web page.

The chapter is structured as follows. The methods of the proposed 3D quantitative image analysis pipeline are detailed in Section 2. Each subsection contains the necessary technical details to understand and reproduce every quantitative imaging biomarkers: intensity-, distance- and texture-based features. Section 3 details the workflows and processes of the proposed online tool, which can be used as a reference manual for the end-user. Conclusions and perspectives are provided in Section 4.

2. Methods

The pipeline of our system is shown in Fig. 12.3. The very first step of the pipeline consists in finding and regrouping image studies and series from a batch zip file uploaded to the server. For each patient, the latter should include Digital Imaging and Communications in Medicine (DICOM) files of both CT and PET scans, as well as a DICOM RT structure file containing the Region(s) Of Interest (ROI) to analyze. The structure of the zip file and its parsing is detailed in Section 3.2. Nonetheless, it is required to explain at this point that the DICOM RT file must contain the ROI corresponding to main tumor referred to as *GTV_T*. Optionally, it may contain secondary ROIs referring to nodes or metastases named *GTV_N*. The structure of the returned CSV file containing all 3D quantitative imaging parameters is described in Section 3.3. The following subsections detail the various steps of the pipeline contained inside the orange box in Fig. 12.3.

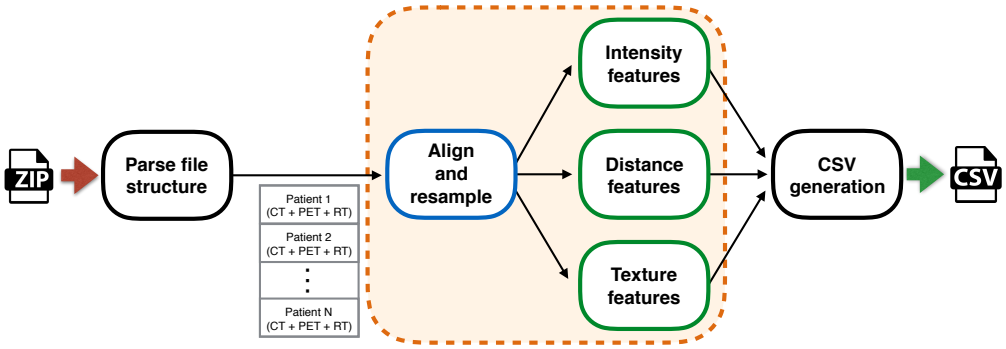

Figure 12.3: Architecture of the proposed 3D quantitative image analysis pipeline.

2.1. PET-CT alignment

The DICOM RT file is generated with respect to the CT scan and the ROI it is always in the same scale and alignment as the CT image. This is not the case for the PET scan. Most often, the resolution of the CT scan is higher than the PET and the volume covered might be unaligned between the two. The volume position and voxel dimensions specified in the headers of the DICOM files series from the PET and CT scans are used to resample and to perform a rigid alignment of the PET series on the CT. This transformation requires an interpolation procedure. The nearest neighbor method is used to preserve the uptake values of the PET. After this step, the PET and CT volumes contain the same number of voxels and cover the same 3-dimensional region. Fig. 12.4 shows a full slice as well as a zoomed view of the around the ROI (marked in green) of fused PET and CT volumes after the alignment. This example will be further used to illustrate the various steps of the system.

2.2. Intensity-based features

This section details intensity-based features, which are based on the regional distributions of the voxel values. The latter correspond to the Hounsfield Units (HU) and the Standardized Uptake Values (SUV) in CT and PET images respectively. Only the voxels inside *GTV_T* and *GTV_N* are used. The system allows to further refine the ROIs based on multiple user-defined metabolic thresholds on the SUV values. This is illustrated in Fig. 12.5, where the initial ROI shown in Fig. 12.4 shrinks with respect to increasing metabolic thresholds τ.

2.2.1. Statistics of voxels values

The first four statistical moments are used to characterize the intensity distribution inside the ROI. By intensity we refer to the voxel values, i.e., HU in CT and SUV in

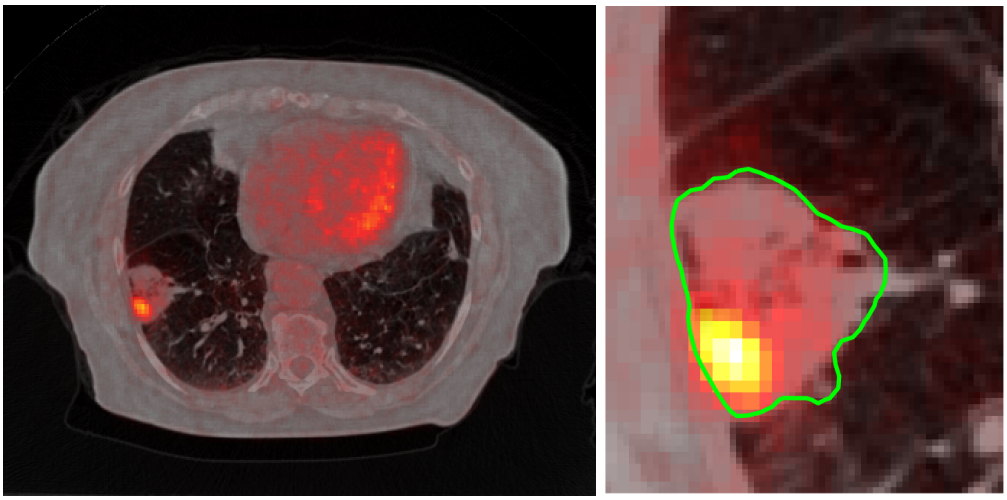

Figure 12.4: Left: axial CT slice and PET image overlay after the alignment and rescaling of the PET image. Right: closeup view of the ROI (green).

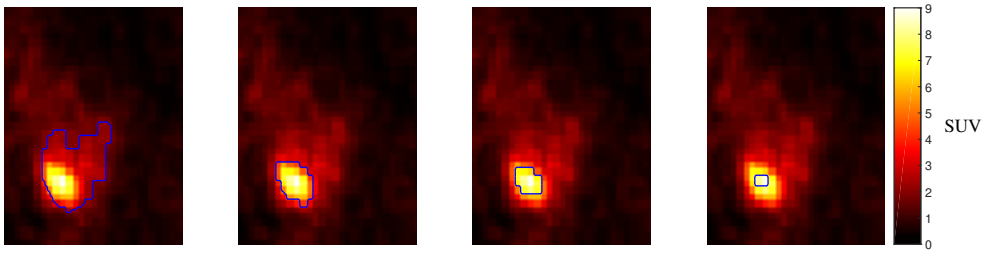

Figure 12.5: Resulting cropped ROI (in blue) when applying increasing metabolic thresholds τ on the initial ROI shown in Fig. 12.4.

PET (see Section 2.1 of Chapter 1). These statistical moments are the mean μ, standard deviation σ, skewness *skew*, and kurtosis *kurt*. Let $\boldsymbol{M}_\tau$ be the region containing the voxels of the ROI $\boldsymbol{M}$ with intensity value greater than a threshold τ. We define $N_{\boldsymbol{M}_\tau}$ as the number of voxels in $\boldsymbol{M}_\tau$. The position of each voxel is determined by the 3D vector $\boldsymbol{\xi}$, and $f(\boldsymbol{\xi})$ corresponds to the intensity value at the position $\boldsymbol{\xi}$. The four moments are defined as

$$\mu_{\boldsymbol{M}_\tau} = \frac{1}{N_{\boldsymbol{M}_\tau}} \sum_{\boldsymbol{\xi} \in \boldsymbol{M}_\tau} f(\boldsymbol{\xi}), \tag{12.1}$$

$$\sigma_{\boldsymbol{M}_\tau} = \sqrt{\frac{1}{N_{\boldsymbol{M}_\tau}} \sum_{\boldsymbol{\xi} \in \boldsymbol{M}_\tau} \left(f(\boldsymbol{\xi}) - \mu_{\boldsymbol{M}_\tau}\right)^2}, \tag{12.2}$$

Table 12.1: Table with the values of the first four moments of the intensity distribution for the examples shown in Fig. 12.6.

	$\mu_{\boldsymbol{M}}$	$\sigma_{\boldsymbol{M}}$	$skew_{\boldsymbol{M}}$	$kurt_{\boldsymbol{M}}$
HU distribution	-78.0416	211.2127	-1.3821	9.4431
Normal distribution	-78.0416	211.2127	0	3
SUV distribution	3.5962	1.9587	1.5430	6.9098
Normal distribution	3.5962	1.9586	0	3

$$skew_{\boldsymbol{M}_\tau} = \frac{1}{N_{\boldsymbol{M}_\tau}\sigma^3_{\boldsymbol{M}_\tau}} \sum_{\boldsymbol{\xi}\in\boldsymbol{M}_\tau} (f(\boldsymbol{\xi}) - \mu_{\boldsymbol{M}_\tau})^3, \tag{12.3}$$

$$kurt_{\boldsymbol{M}_\tau} = \frac{1}{N_{\boldsymbol{M}_\tau}\sigma^4_{\boldsymbol{M}_\tau}} \sum_{\boldsymbol{\xi}\in\boldsymbol{M}_\tau} (f(\boldsymbol{\xi}) - \mu_{\boldsymbol{M}_\tau})^4. \tag{12.4}$$

The skewness measures the symmetry of the distribution. $skew = 0$ means that the distribution is symmetric, $skew < 0$ means that the distribution is more concentrated on the right of the mean μ (*i.e.*, high voxel values), and $skew > 0$ when the concentration is on the left of the μ. The kurtosis measures the tailedness of the distribution, *i.e.*, the concentration of the data around μ. The higher is the kurtosis, the more concentrated the data with a high peak at μ. The normal distribution has always $skew = 0$ because it is completely symmetric. Its kurtosis is always 3. Fig. 12.6 shows the distributions of the CT (HU) and PET (SUV) inside the unthresholded ROI $\boldsymbol{M}$ shown in Fig. 12.4. The normal distribution with identical μ and σ as the corresponding distribution is showed in black to illustrate the significance of skewness and kurtosis. The intensity statistics of $\boldsymbol{M}$ are specified in Table 12.1.

2.2.2. PET-specific intensity-based features

A set of PET-specific features based on the distribution of SUV intensity values has been identified in the literature as meaningful for assessing the metabolic properties of tumors [50, 8]. These are (i) SUV_{max}, the maximum SUV value inside the ROI, (ii) SUV_{peak}, the peak SUV measuring the mean SUV value within a spherical neighborhood of 1.2 cm radius and centered at the position of SUV_{max}, (iii) *MTV*, the Metabolic Tumor Volume, and (iv) *TLG*, the Total Lesion Glycolysis combining both metabolic and volumetric information. Let $\boldsymbol{S}_{\text{max}}$ be the spherical neighborhood of SUV_{max}, and v_{vox} the volume of one single voxel. The measures are defined as (following the notation introduced in Section 2.2.1)

$$SUV_{\text{max}} = \max_{\boldsymbol{\xi}\in\boldsymbol{M}}(f(\boldsymbol{\xi})), \tag{12.5}$$

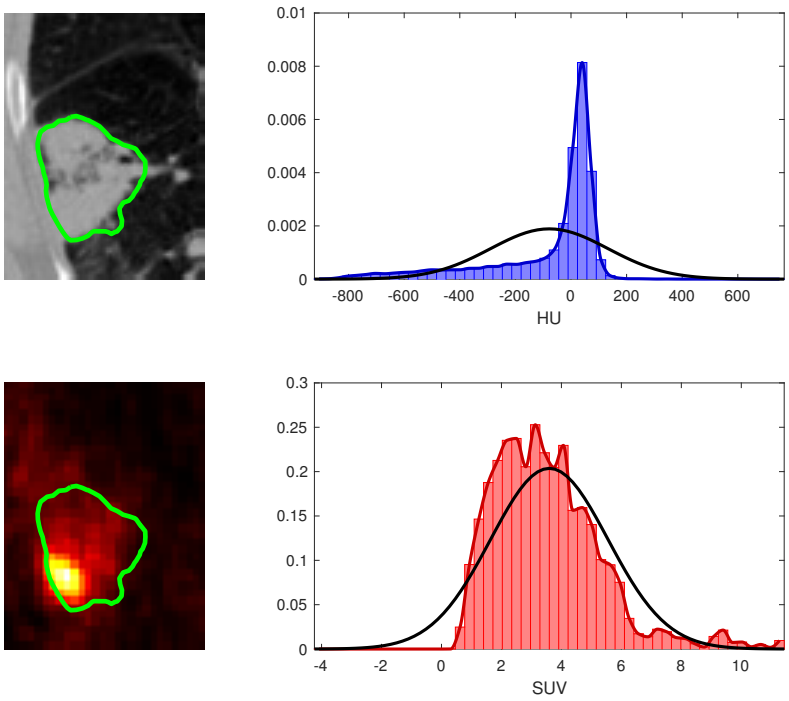

Figure 12.6: Distribution curves for each intensity measure in CT (top) and PET (bottom). The equivalent normal distributions with corresponding μ and σ are shown in black.

$$SUV_{\text{peak},\tau} = \frac{1}{N_{\boldsymbol{M}_\tau \cap \boldsymbol{S}_{\max}}} \sum_{\boldsymbol{\xi} \in \boldsymbol{M}_\tau \cap \boldsymbol{S}_{\max}} f(\boldsymbol{\xi}) = \mu_{\boldsymbol{M}_\tau \cap \boldsymbol{S}_{\max}}, \tag{12.6}$$

$$MTV_\tau = v_{\text{vox}} \cdot N_{\boldsymbol{M}_\tau}, \tag{12.7}$$

$$TLG_\tau = \mu_{\boldsymbol{M}_\tau} \cdot MTV_\tau. \tag{12.8}$$

It worth noting that $SUV_{\max}$ is not affected by the threshold τ.

2.3. Distance features: measures of cancer invasiveness

Fried *et al.* introduced the concept of *disease solidity* for NSCLC in [23]. It consists of measuring disease spread by computing the relation between the volume of the main tumor and all secondary nodes with respect to the volume of their convex hull. The latter is defined as the smallest convex shape containing all nodules (including the tumor). Following this concept, we designed new measures of metastases spread based on dis-

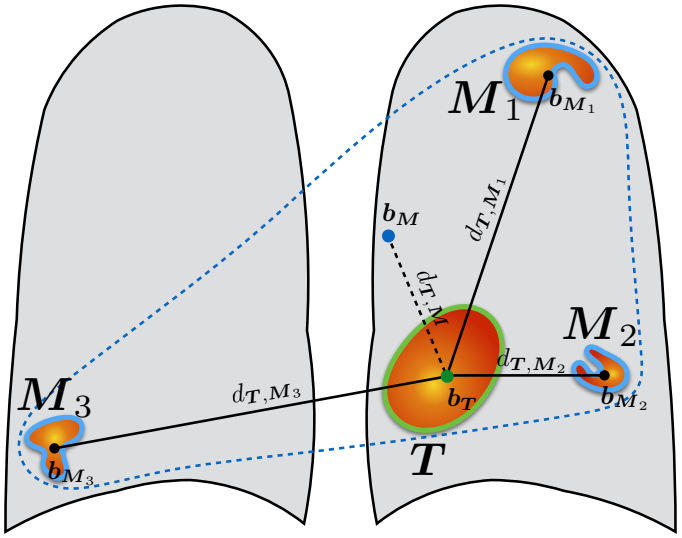

Figure 12.7: Distances features as measures of cancer invasiveness. Various distances $d_{\boldsymbol{T},\boldsymbol{M}_i}$ between the barycenter $b_{\boldsymbol{T}}$ of the primary tumor region $\boldsymbol{T}$ and the barycenter $b_{\boldsymbol{M}_i}$ of each metastasis region $\boldsymbol{M}_i$ are computed to measure the spread of disease.

tances between the main tumor (delimited in *GTV_T*) and the metastases (in *GTV_N*). The various distance measures are illustrated in Fig. 12.7. Let $\boldsymbol{T}$ be volumetric region of the main tumor and $\boldsymbol{M}_i$ the region of metastasis i. Let $\boldsymbol{b}_{\boldsymbol{T}}$ be the barycenter of the main tumor, $\boldsymbol{b}_{\boldsymbol{M}_i}$ the barycenter of the metastasis i, and $\boldsymbol{b}_{\boldsymbol{M}}$ the barycenter of all metastases. The distance between $\boldsymbol{T}$ and $\boldsymbol{M}_i$ is defined as the Euclidean distance between their barycenters, *i.e.*

$$d_{\boldsymbol{T},\boldsymbol{M}_i} = \|\boldsymbol{b}_{\boldsymbol{T}} - \boldsymbol{b}_{\boldsymbol{M}_i}\|_2 \tag{12.9}$$

The same formula is used to compute the distance between the main tumor and the barycenter of all metastases $d_{\boldsymbol{T},\boldsymbol{M}}$. Considering this definition, and denoting the MTV in cubic millimeters (mm^3) of the metastasis $\boldsymbol{M}_i$ as MTV_i, seven different features are introduced as

(i) the distance between the tumor and the barycenter of all metastases $\boldsymbol{b}_{\boldsymbol{M}}$

$$d_{\boldsymbol{T},\boldsymbol{M}} = \|\boldsymbol{b}_{\boldsymbol{T}} - \boldsymbol{b}_{\boldsymbol{M}}\|_2, \tag{12.10}$$

(ii) the sum of all tumor-metastasis distances

$$\sum_i d_{\boldsymbol{T},\boldsymbol{M}_i} = \sum_i \|\boldsymbol{b}_{\boldsymbol{T}} - \boldsymbol{b}_{\boldsymbol{M}_i}\|_2, \tag{12.11}$$

(iii) the sum of distances weighted by the respective MTV of the metastases

$$\sum_i MTV_i \cdot d_{\boldsymbol{T},\boldsymbol{M}_i} = \sum_i MTV_i \cdot \|\boldsymbol{b}_{\boldsymbol{T}} - \boldsymbol{b}_{\boldsymbol{M}_i}\|_2, \tag{12.12}$$

(iv) the metastasis remoteness

$$\max_i \{d_{\boldsymbol{T},\boldsymbol{M}_i}\} = \max_i \{\, \|\boldsymbol{b}_{\boldsymbol{T}} - \boldsymbol{b}_{\boldsymbol{M}_i}\|_2\}\,, \tag{12.13}$$

(v) the metastasis remoteness weighted by the MTV of the corresponding metastasis

$$\max_i \{MTV_i \cdot d_{\boldsymbol{T},\boldsymbol{M}_i}\} = \max_i \{MTV_i \cdot \|\boldsymbol{b}_{\boldsymbol{T}} - \boldsymbol{b}_{\boldsymbol{M}_i}\|_2\}\,, \tag{12.14}$$

(vi) the cumulative distance between each metastasis and the barycenter of all metastases

$$\sum_i d_{\boldsymbol{M}_i,\boldsymbol{M}} = \sum_i \|\boldsymbol{b}_{\boldsymbol{M}_i} - \boldsymbol{b}_{\boldsymbol{M}}\|_2, \tag{12.15}$$

and (vii) the MTV-weighted version of the latter

$$\sum_i MTV_i \cdot d_{\boldsymbol{M}_i,\boldsymbol{M}} = \sum_i MTV_i \cdot \|\boldsymbol{b}_{\boldsymbol{M}_i} - \boldsymbol{b}_{\boldsymbol{M}}\|_2. \tag{12.16}$$

2.4. Texture features

Another set of quantitative imaging features extracting measures of 3D texture, *i.e.*, the spatial transitions between the voxel values (see Section 2.1 of Chapter 1) are implemented. The three main groups of texture measures are 3D Gray-Level Co-occurrence Matrices (GLCM) [34], 3D Laplacians of Gaussians (LoG), and 3D Riesz wavelets [12]. Detailed descriptions and review can be found in Sections 3.1, 2.1 and 2.2 of Chapter 3, respectively. The latter were successfully used in various radiomics applications [24, 22, 18, 19, 13].

2.4.1. Isometric volumes

Inside the body, three-dimensional tissue architectures can be constituted of texture patterns characterized by transitions between voxel values along any directions of $\mathbb{R}^3$. To ensure the unbiased management of directions, the voxels of the images must be isometric, *i.e.*, the dimensions of each voxel $\Delta\xi_1$, $\Delta\xi_2$, $\Delta\xi_3$ must be equal (see Section 3.2 and Fig. 1.15 of Chapter 1). Moreover, the voxel dimensions must be normalized across patients to allow optimal inter-patient comparisons of image scales and directions. As a pre-processing step before extracting any texture feature, CT, PET, and ROI volumes are resampled to have identical isometric voxel sizes. The latter are set to $0.75 \times 0.75 \times 0.75$ mm^3 as a trade-off between data size and image resolution. Resampling methods are based on cubic spline interpolation for the CT volume and on nearest neighbors for PET and ROI volumes.

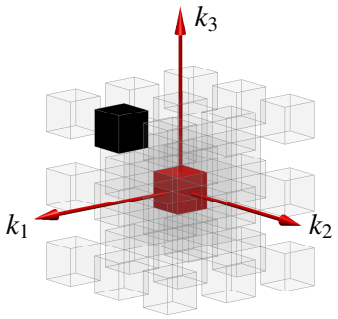

Figure 12.8: 3D GLCM neighborhood of all possible spatial configurations between the central voxel (red) and another voxel (semi-transparent) separated by a distance of 1 and 2 voxels. A displacement parameterized by the index vector $\Delta\boldsymbol{k} = (\Delta k_1 = 2, \Delta k_2 = 1, \Delta k_3 = 2)$ is exemplified between the black voxel and the center one (red).

2.4.2. 3D gray level co-occurrence matrix (GLCM) features

GLCMs constitute a group of popular texture descriptors introduced by Haralick *et al.* in [34]. The 2D version of this descriptor is discussed in Section 3.1 of Chapter 3. 3D GLCMs were proposed for the description of 3D textures in [53, 14]. The properties of 2D GLCMs presented in Table 3.8 of Chapter 3 are also valid for the 3D extension. 3D GLCMs are extending their 2D counterparts consisting in measuring the co-occurrences between two voxel values in a 3D neighborhood. Fig. 12.8 shows the 3D neighborhood of all possible spatial configurations between the central voxel (red) and another voxel (semi-transparent) separated by a distance of 1 and 2 voxels. While the set of 2D directions $\boldsymbol{u}$ can be defined with one single angle θ in polar coordinates, $\boldsymbol{u}$ is parameterized by 2 angles (θ, ϕ) in spherical coordinates (see Section 2 of Chapter 2). The 13 equally-sampled directions used to approximate the full 3D neighborhood are detailed in Table 12.2 (see Fig. 1.14 of Chapter 1). The cumulative co-occurrences along every 13 directions allow building approximately locally rotation-invariant features in a similar fashion as 2D locally rotation-invariant GLCMs depicted in Fig. 3.10 of Chapter 3. This strategy has been commonly used in the literature [16]. 11 texture measurements are computed from the GLCMs to characterize 3D texture properties. These are: *contrast*, *correlation*, *energy*, *homogeneity*, *entropy*, *inverse different moment*, *sum average*, *sum entropy*, *sum variance*, *difference variance* and *difference entropy* (detailed formula can be found in [33]). The *contrast* and *energy* texture features correspond to our intuitive perception of texture in 2D.

Table 12.2: The thirteen 3D directions $\boldsymbol{u}$ considered for computing GLCMs.

Coordinates of $\boldsymbol{u} \in \mathbb{R}^3$	θ	ϕ
(0, 1, 0)	$\frac{\pi}{2}$	0
(1, 1, 0)	$\frac{\pi}{4}$	0
(1, 0, 0)	0	0
(1, -1,0)	$-\frac{\pi}{4}$	0
(0, 1, 1)	$\frac{\pi}{2}$	$\frac{\pi}{4}$
(0, 0, 1)	0	$\frac{\pi}{2}$
(0, -1, 1)	$-\frac{\pi}{2}$	$\frac{3\pi}{4}$
(1, 1, 1)	$\frac{\pi}{4}$	$\frac{\pi}{4}$
(1, 0, 1)	0	$\frac{\pi}{4}$
(1, -1, 1)	$-\frac{\pi}{4}$	$\frac{\pi}{4}$
(1, 1, -1)	$\frac{\pi}{4}$	$-\frac{\pi}{4}$
(1, 0, -1)	0	$-\frac{\pi}{4}$
(1, -1, -1)	$-\frac{\pi}{4}$	$-\frac{3\pi}{4}$

2.4.3. 3D Laplacian of Gaussians (LoG) features

One of the simplest texture descriptor based on convolution is the Laplacian of Gaussians (LoG). The LoG operator is defined for any D-dimensional image in Section 2.1 of Chapter 3. The formula of the operator function is specified in Eq. (3.5) and its main properties are summarized in Table 3.1. The parameter controlling the size of the LoG filters is σ and allows studying volumetric texture properties at multiple scales. This σ is referred in this section as σ_{LoG} to distinguish it from the standard deviation of intensity distributions introduced in Section 2.2.1. A set of multi-scale and locally rotation-invariant (LoG are circularly/spherically symmetric) texture measurements is obtained by averaging the absolute values of the response maps of LoG operators in the ROI mask $\boldsymbol{M}$ for a series of increasing values of σ_{LoG}. Fig. 12.9 depicts the profile of the LoG filter for three different σ_{LoG} values. The response maps resulting from the convolutions of the three filters with two different images f_A and f_B are shown in Fig. 12.10. It can be observed that different values of σ_{LoG} can be used to characterize different texture scales.

As described in Fig. 1.12 of Chapter 1, it is possible to distinguish between the texture found on the margin of the ROI ($\boldsymbol{M}_{\text{margin}}$) and the one found in the core region of the tumor ($\boldsymbol{M}_{\text{core}} \equiv GTV\_N$). To that end, the LoG response maps are averaged in both regions separately (see Fig. 12.11). $\boldsymbol{M}_{\text{margin}}$ is obtained from the difference between $\boldsymbol{M}_{\text{core}}$ dilated and eroded with a spherical structural element (diameter = 2.25mm). Therefore, the tumor margin has an approximate thickness of 4.5mm.

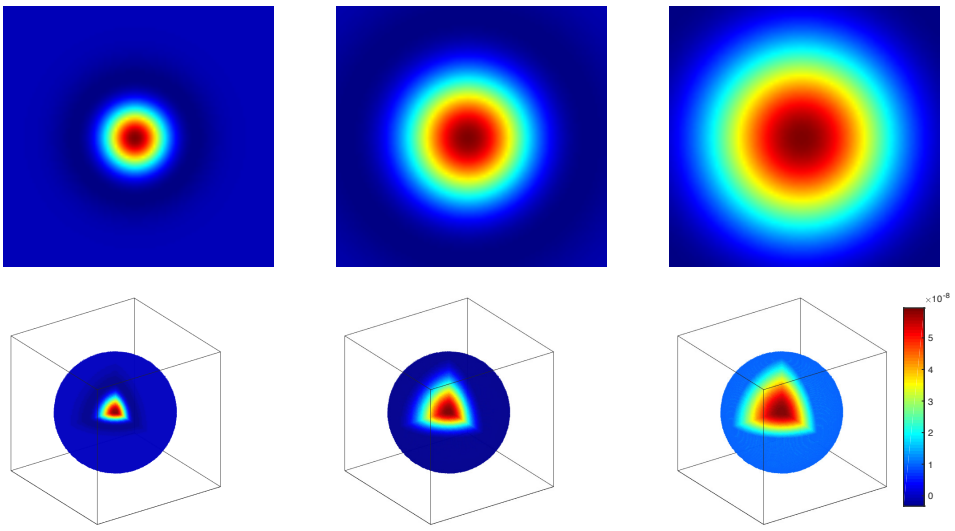

Figure 12.9: 3D LoG filters at various scales controlled by the parameter σ_{LoG}. The top row shows central sections of the filters and the bottom row shows spherical wedges.

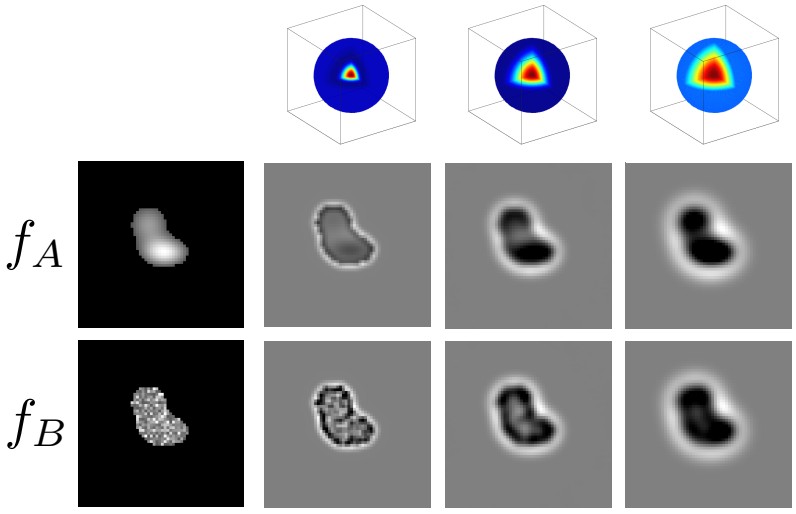

Figure 12.10: 2D sections of the response maps of two different simulated tumors f_A and f_B for the LoG filters shown in Fig. 12.9.

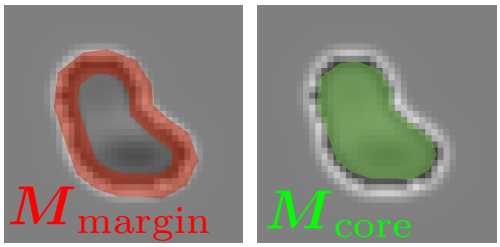

Figure 12.11: $\boldsymbol{M}_{\text{margin}}$ and $\boldsymbol{M}_{\text{core}}$ regions used for feature aggregation.

2.4.4. 3D Riesz-wavelets features

Another convolutional feature group is extracted by the proposed pipeline and is based on 3D Riesz wavelets [12]. The latter are defined for any D-dimensional image and are detailed in Section 2.2 of Chapter 3. They consist in computing the real Riesz transform of a primal circularly/spherically symmetric wavelet decomposition, the latter being similar to LoG filters. The Lth-order real Riesz transform of an image $f(\boldsymbol{x})$ computes Lth-order all-pass derivatives of the latter. In other words, $L = 1$ computes first-order image derivatives and measures the slope of the spatial transition between the values of a set of aligned voxels, and the second-order transform ($L = 2$) measures the curvature of the transition. Consequently, they have an intuitive interpretation and have shown to provide relevant quantitative image measurements in the context of several medical applications [13, 17, 19, 6, 15, 51]. We used the primal circularly/spherically symmetric wavelet presented in [18, 55], which was found to have an optimal bandwidth. We limited a maximum Riesz order to 2 and a maximum of wavelet scales to 4. Riesz order 1 encodes the gradient of the image (first order derivative), while order 2 also encodes the Hessian of the image (second order derivative). The scale controls the size of the texture properties to be detected. Fig. 12.12 shows sliced response maps of first-order Riesz wavelets for scale 1 and 2 on a 2D slice of the synthetic tumor f_B (see Fig. 12.10). While the LoG reacts equally to transitions between voxel values along any direction (LoGs are circularly/spherically symmetric), the first-order Riesz filterbank contains three different filters characterizing three orthogonal directions. Second-order Riesz filters characterize six different directions according to the Hessian (see Fig. 12.13). Sets of scalar texture measurements are obtained by computing the average energies of the response maps in both the tumor margin $\boldsymbol{M}_{\text{margin}}$ and the core $\boldsymbol{M}_{\text{core}}$ region (see Fig. 12.11).

In order to obtain both directional and locally rotation-invariant features, Riesz wavelets are aligned at each position $\boldsymbol{\xi}_0$ based on the local direction $\boldsymbol{u}$ maximizing the energy of the gradient [20, 12]. This alignment strategy is applicable to any Riesz order and is illustrated in Fig. 12.14) for order 1 (*i.e.*, the gradient). The benefits of locally aligning the filters are explained in Section 4.3 (moving frames) of Chapter 2

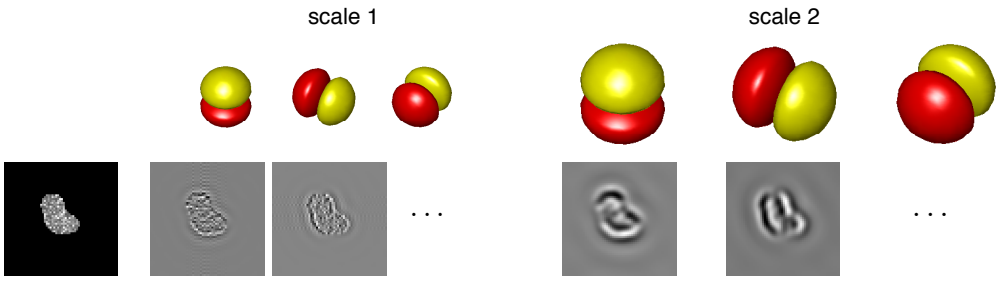

Figure 12.12: Response maps of the simulated tumor image f_B (left) for Riesz filterbanks of order 1 with scales 1 and 2.

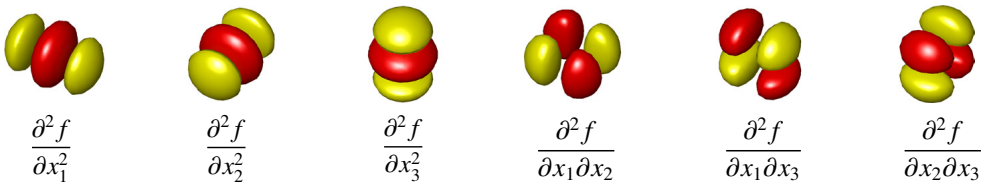

Figure 12.13: Profiles of the elements the Riesz filterbank of order 2. The latter corresponds to the six distinct second-order derivatives (*i.e.*, the Hessian) of the circularly/spherically symmetric primal wavelet.

for 2D images. This local alignment is even more important in 3D as the amount of possible directions is much larger in volumetric neighborhoods. To demonstrate the importance of locally aligning the filters, we designed a synthetic example of possible local volumetric tissue architecture. The latter follows the examples provided in Section 4.1 of Chapter 2 showing two-dimensional natural and biomedical textures where the local organization of the image directions (LOID) is crucial for their unequivocal description (see Fig. 2.10). Our example extends the latter to 3D and contains three volumetric solid images with three tubular bars each (see Fig. 12.15). They simulate tubular structures crossing in the 3D space as it may occur with *e.g.*, intricate tissue vasculature. The importance of maintaining the directional information while obtaining locally rotation-invariant features is demonstrated in Fig. 12.16, where the discriminatory power of the various texture features, *i.e.*, 3D GLCMs (see Section 2.4.2), 3D LoGs (see Section 2.4.3), and aligned 3D Riesz wavelets are compared. GLCMs and LoGs yield almost identical feature values for the three synthetic images, while the aligned Riesz filters are able to discriminate each of them. For this example, seven values of σ_{LoG} were used for the LoG filters. Order 2 and one scale were used for the Riesz wavelets.

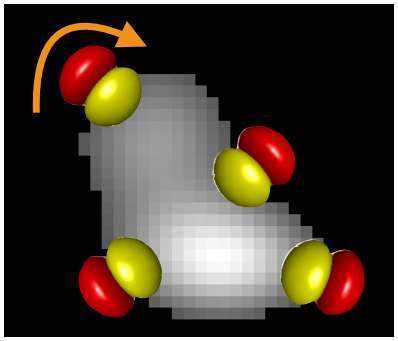

Figure 12.14: Illustration of the local alignment strategy of the Riesz filters on the boundary of a synthetic tumor. Riesz wavelets of order 1 are depicted.

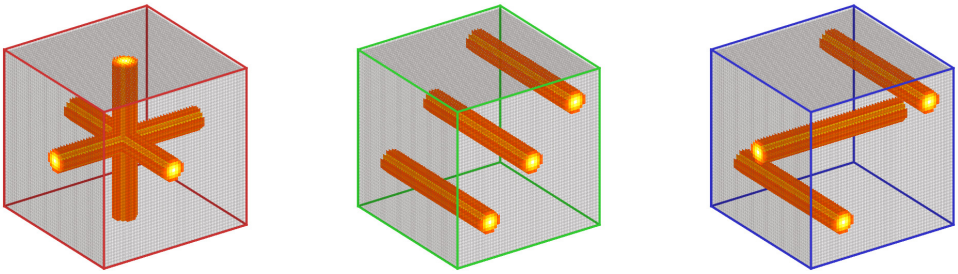

Example 1 Example 2 Example 3

Figure 12.15: Synthetic 3D images containing three tubular structures with varying spatial configurations. The latter simulate, *e.g.*, possible vascular structures.

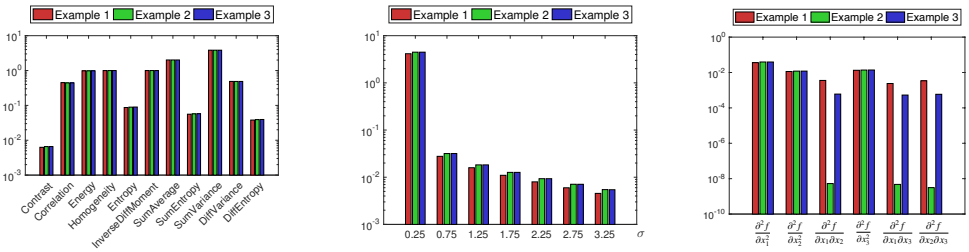

3D GLCMs 3D LoGs aligned 3D Riesz

Figure 12.16: Feature values obtained for the three examples shown in Fig. 12.15. Only aligned Riesz wavelets are able to discriminate each of them.

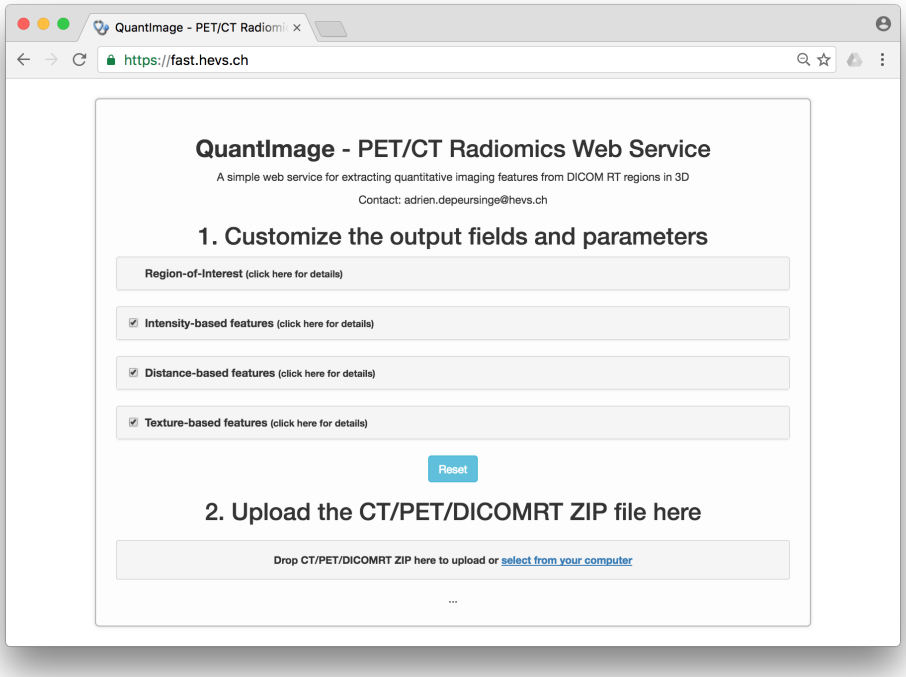

Figure 12.17: Home page of QuantImage, which can be accessed at `https://radiomics.hevs.ch`.

3. The QuantImage online image analysis platform

The QuantImage online platform consists of a simple web-page where the physicians can upload batches of image series from multiple patients and download a CSV file containing the values of the features described in the previous sections. The underlying system of the developed web-service follows the pipeline depicted in Fig. 12.3. It mainly consists of three steps from a user point of view: choosing system parameters, uploading DICOM files, and downloading the computed features. These three steps were carefully designed to be user-friendly and based on default parameter values, while users can also have the full control of the computed features and their parameterizations. The home page of QuantImage can be accessed at `https://radiomics.hevs.ch` and is depicted in Fig. 12.17.

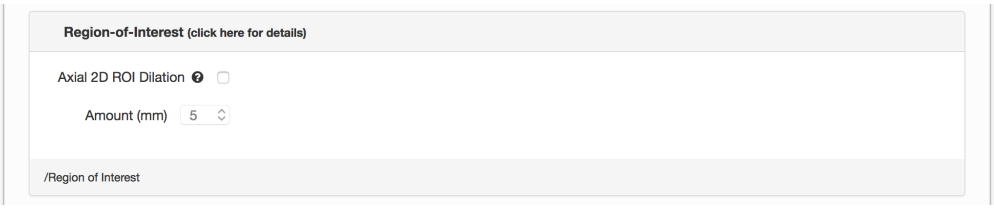

Figure 12.18: Options for performing axial-wise dilations of GTV_N ROIs provided in the DICOM RT files.

3.1. Parameter setting

As a first step, the user can select the parameter values for the QuantImage computing pipeline. The latter are grouped in four consecutive blocks. The first block allows performing an initial dilation (in mm) of the ROIs (GTV_T and GTV_N). The ROI named GTV_T corresponds to the delineation of the main tumor (see Fig. 12.18), while GVT_N refers to secondary nodules. This optional dilation is performed in 2D for each axial slice of GTV_T and GTV_N. It is useful when the initial ROIs provided in the DICOM RT files do not cover the full tumor volumes. The subsequent metabolic thresholds τ will yield more precise metabolic subregions. The three following blocks refer to each feature group described in Sections 2.2, 2.3, 2.4 and are detailed in Sections 3.1.1, 3.1.2, 3.1.3, respectively.

3.1.1. Intensity-based features parameters

The second block of the QuantImage web page allows choosing whether to extract the various intensity-based features and their parameters. A clickable question mark icon is available next to each option to obtain more information about the type of feature and its parameters. The features are organized in two subgroups: *CT Measures* and *PET Measures*. *CT Measures* refer to the mean HU inside the main tumor GTV_T and is computed at two different metabolic thresholds τ_i based on the PET image (see Section 2.2.1). These are $\tau_1 = 3$ SUV and $\tau_2 = 42\%$ of $SUV_{\max}$. The *PET Measures* correspond to the statistics and PET-specific features described in Sections 2.2.1 and 2.2.2, respectively. In this case, the user can define sets of metabolic thresholds by setting the range of values of τ and an incremental step. These thresholds can be specified for measures extracted from both the main tumor GTV_T and from other nodes GTV_N (when available in the DICOM RT files). This selection can be specified for both absolute SUV values and relative to $SUV_{\max}$. For intensity measures computed from GTV_N with relative thresholds, the reference $SUV_{\max}$ can be computed from either GTV_T or GTV_N.

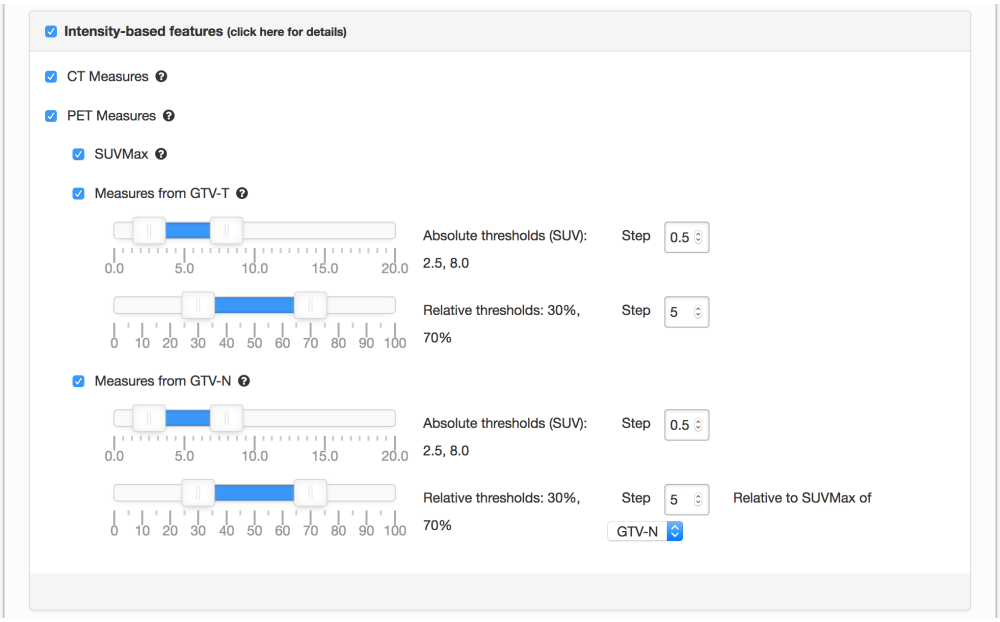

Figure 12.19: Parameter setting for intensity features.

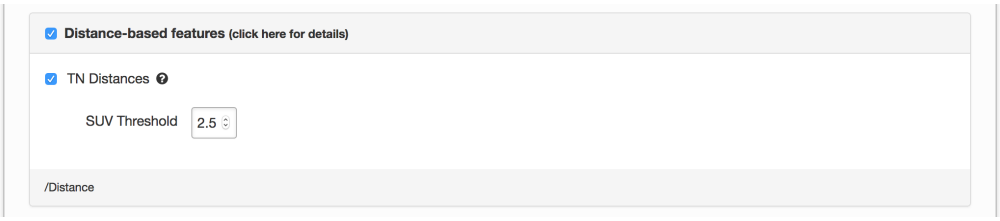

Figure 12.20: Parameter setting for distance features.

3.1.2. Distance-based features parameters

The only parameter to set for distance based features is the metabolic threshold for all GTV regions. The features computed when this option is selected are described in Section 2.3.

3.1.3. Texture-based features parameters

The last block is dedicated to the parameter setting of the texture-based features described in Section 2.4 (3D GLCMs, 3D LoGs, and 3D Riesz). Only the most important parameters of the descriptors can be tuned to limit the complexity of use. The texture features are extracted from both CT and PET image series inside *GTV_T*. In the case of the GLCMs, the user can choose whether to consider symmetric voxel pairs, the dis-

Figure 12.21: Parameter setting for 3D texture features.

tance between voxels, and the number of gray levels (see Section 2.4.2). The features returned for this descriptor are the 11 measures mentioned previously. When selecting 3D LoGs, the user must select the range of scales parameterized by σ_{LoG} in between 0.25 and 3.25 with a fixed step of 0.5. As explained in Section 2.4.3, these features are computed from both the core and the margin of the ROI. The last section of this block concerns the parameter setting for Riesz wavelets, *i.e.*, the order of the image derivatives and the number of scales. The Riesz energy features are computed from both the core and the margin of the ROI.

3.2. File upload

Once the parameters are defined by the user, the next step is to upload the DICOM files of the batch of patients to be analyzed on the server. This file transfer includes encryption to protect patient data. The user must provide one unique zip file containing all CT, PET, and DICOM RT files of all patients. The files must be all DICOM files (CT and PET), and DICOM RT (ROI). The file structure inside the zip file is not important, because the system is able to parse the inner structure of the zip file by reading the DICOM headers and to regroup files based on patients and image series. The DICOM RT file must at least include one ROI named *GTV_T* corresponding to the main tumor. It may contain another optional ROI named *GTV_N* with other nodes of interest (*e.g.*, metastasis regions). If no *GTV_N* ROI is provided, the corresponding features will not be computed and will have *NaN* (not a number) values in the returned CSV data structure. After creating the zip file containing the above-mentioned files,

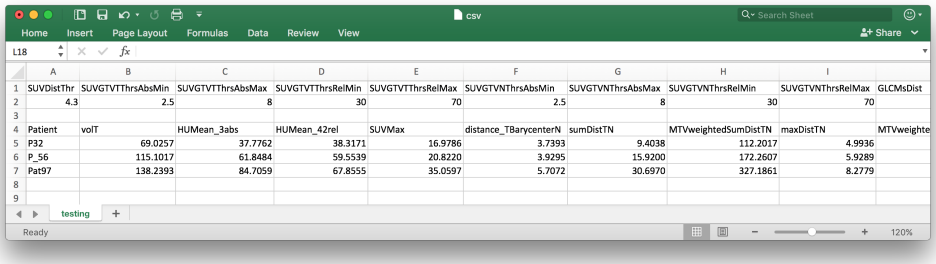

	A	B	C	D	E	F	G	H	I	
1	SUVDistThr	SUVGTVTThrsAbsMin	SUVGTVTThrsAbsMax	SUVGTVTThrsRelMin	SUVGTVTThrsRelMax	SUVGTVNThrsAbsMin	SUVGTVNThrsAbsMax	SUVGTVNThrsRelMin	SUVGTVNThrsRelMax	GLCMsDist
2	4.3	2.5	8	30	70	2.5	8	30	70	
3										
4	Patient	volT	HUMean_3abs	HUMean_42rel	SUVMax	distance_TBarycenterN	sumDistTN	MTVweightedSumDistTN	maxDistTN	MTVweighte
5	P32	69.0257	37.7762	38.3171	16.9786	3.7393	9.4038	112.2017	4.9936	
6	P_56	115.1017	61.8484	59.5539	20.8220	3.9295	15.9200	172.2607	5.9289	
7	Pat97	138.2393	84.7059	67.8555	35.0597	5.7072	30.6970	327.1861	8.2779	
8										
9										

Figure 12.22: Screenshot of the resulting CSV data structure returned by the system. In this particular case, three patients with identifiers "P32", "P_56" and "Pat96" were processed (see lines 5-7). The parameter values used for feature extraction are displayed in lines 1 and 2.

the user can upload it in the block entitled "2. Upload the CT/PET/DCOMRT ZIP file here" shown in Fig. 12.17. The upload can be done either by browsing the file system or with a simple drag-and-drop. After clicking the button upload, a progress bar will show the progress of file upload, followed by the progress of file processing and feature extraction.

3.3. Output CSV data structure

The output of the web-service is a CSV file containing the feature values. The first two rows of the file contain the values of the parameters chosen by the user, allowing reproducibility of the experiments. The next non-empty row of the file contains a header with the names of the computed features. Each following row corresponds to each single patient included in the uploaded zip file. Tables .4, .5, .6, .7, and .8 in the Appendix detail the various feature names used and their signification. In order to shorten the list of names, we used the following naming conventions in the feature-code field:

- a list of strings in between { } means that one and only one string can be present in the final name,
- a letter in between [ ] means that this letter corresponds to a parameter and it will be encoded by its substituted value,
- a parameter called *charDir* was included for Riesz features that will be replaced by the composition of the letters X, Y and Z, representing the direction of the Riesz filter following the partial directional image derivatives (*e.g.*, XX corresponds to $\partial^2/\partial x_1^2$, XY corresponds to $\partial^2/\partial x_1 \partial x_2$).

Table 12.3: Variations of the feature-code *tex_InnerRieszN[n]_*{CT,PET}*_[*charDir*]_scale[s]* when using Riesz wavelets of order 2 and 2 consecutive scales.

tex_InnerRieszN2_CT_XX_scale1	tex_InnerRieszN2_CT_YY_scale1	tex_InnerRieszN2_CT_ZZ_scale1
tex_InnerRieszN2_CT_XY_scale1	tex_InnerRieszN2_CT_XZ_scale1	tex_InnerRieszN2_CT_YZ_scale1
tex_InnerRieszN2_CT_XX_scale2	tex_InnerRieszN2_CT_YY_scale2	tex_InnerRieszN2_CT_ZZ_scale2
tex_InnerRieszN2_CT_XY_scale2	tex_InnerRieszN2_CT_XZ_scale2	tex_InnerRieszN2_CT_YZ_scale2
tex_InnerRieszN2_PET_XX_scale1	tex_InnerRieszN2_PET_YY_scale1	tex_InnerRieszN2_PET_ZZ_scale1
tex_InnerRieszN2_PET_XY_scale1	tex_InnerRieszN2_PET_XZ_scale1	tex_InnerRieszN2_PET_YZ_scale1
tex_InnerRieszN2_PET_XX_scale2	tex_InnerRieszN2_PET_YY_scale2	tex_InnerRieszN2_PET_ZZ_scale2
tex_InnerRieszN2_PET_XY_scale2	tex_InnerRieszN2_PET_XZ_scale2	tex_InnerRieszN2_PET_YZ_scale2

As an example, let us consider the following feature-code

*tex_InnerRieszN[n]_*{CT,PET}*_[*charDir*]_scale[s].*

Let then suppose that the user selected a Riesz order of 2, and 2 wavelet scales. Then, this feature-code will be denoted in the CSV file with all the forms listed in Table 12.3.

4. Discussions and conclusions

We presented an online radiomics tool called QuantImage. The latter is based on a user-friendly web-service allowing the extraction of current state-of-the-art three-dimensional quantitative imaging features from PET and CT images. To the best of our knowledge, this is the first radiomics-specific tool that can be simply accessed through a secure web platform. The latter enables the extraction of quantitative imaging parameters from large cohorts of patients without the need of neither software nor hardware installation. The online tool can therefore be accessed directly from a clinical environment. We believe that this effort is timely to further validate the relevance of radiomics imaging biomarkers with large-scale clinical studies in the context of well-defined and well-controlled oncological contexts. The features extracted by the system include intensity-, distance-, and texture-based descriptors. While all feature groups are preconfigured with default parameter values, the user has the possibility to further choose which features to extract and to tune their most important parameters. The most relevant aspects of these features are explained in this chapter, which can be used as a reference manual of the QuantImage system. The output of the system is in the standard CSV data format, offering the possibility to manually analyze the feature values with data plots, as well as their inclusion in more complex systems including advanced uni- and multi-variate statistical methods or machine learning techniques such data clustering, linear discriminant analysis, LASSO regression or support vector machines to name a few. Whereas all intensity- and texture-based

Table .4: Feature-codes used for general information in the CSV file.

Feature-code	Description
Patient	Patient ID found in DICOM header.
volT	Volume of *GTV_T*.

quantitative imaging features were previously validated in various applicative contexts [13, 19, 2, 45, 5, 46, 2, 54, 42, 25, 24, 27, 26, 43, 4, 35, 11, 38, 39, 29, 37, 49, 7, 3]. The presented system was initially validated in the context of head and neck [8, 10, 9] tumors at the Lausanne University Hospital (CHUV). Future work includes the implementation of covariance-based aggregation functions as an alternative to the average for LoGs and Riesz wavelets [13], as well as three-dimensional shape features for the characterization of the tumoral contour.

Appendix

This section details the various feature names and their signification as listed in the CSV data structure returned by the system. General information, intensity (parts I and II), distance and texture feature-codes are detailed in Tables .4, .5, .6, .7, and .8, respectively.

Acknowledgments

This work was partly supported by the Swiss National Science Foundation with grant agreements 320030–146804 and PZ00P2_154891, and the CIBM.

Bibliography

1. Hugo J. W. L. Aerts, Emmanuel Rios Velazquez, Ralph T. H. Leijenaar, Chintan Parmar, Patrick Grossmann, Sara Carvalho, Johan Bussink, René Monshouwer, Benjamin Haibe-Kains, Derek Rietveld, Frank Hoebers, Michelle M Rietbergen, Andre Leemans, C Renéand Dekker, John Quackenbush, Robert J Gillies, and Philippe Lambin. Decoding tumour phenotype by noninvasive imaging using a quantitative radiomics approach. *Nature Communications*, 5, June 2014.
2. Omar S. Al-Kadi, Dimitri Van De Ville, and Adrien Depeursinge. Multidimensional texture analysis for improved prediction of ultrasound liver tumor response to chemotherapy treatment. In *Medical Image Computing and Computer-Assisted Interventions (MICCAI)*, volume 9900, pages 619–626. Springer International Publishing, 2016.
3. S Allin Christe, B Vasantha Kumari, and A Kandaswamy. Experimental study for 3D statistical property based intracranial brain tumor classification. *Journal of Scientific and Industrial Research*, 71(1):36–44, 2012.
4. Samson B. Antel, D. Louis Collins, Neda Bernasconi, Frederick Andermann, Rajjan Shinghal, Robert E. Kearney, Douglas L. Arnold, and Andrea Bernasconi. Automated detection of focal cortical dysplasia lesions using computational models of their MRI characteristics and texture analysis. *NeuroImage*, 19(4):1748–1759, August 2003.
5. Imon Banerjee, Sadhika Malladi, Daniela Lee, Adrien Depeursinge, Melinda Telli, Jafi Lipson,

Table .5: Feature-codes for intensity features used in the CSV file (part I): features extracted in ROI GTV_T

Feature-code	**Description**
int_HUMean_3abs	Mean HU of the main tumor voxels with SUV >3.
int_HUMean_42rel	Mean HU of the main tumor voxels with SUV >42 % of SUVMax.
int_SUVMax	Maximum SUV inside the main tumor.
int_SUVMean_T_[τ]abs	Mean SUV of the main tumor voxels with SUV >τ.
int_SUVVariance_T_[τ]abs	SUV variance of the main tumor voxels with SUV >τ.
int_SUVSkewness_T_[τ]abs	SUV skewness of the main tumor voxels with SUV >τ.
int_SUVKurtosis_T_[τ]abs	SUV kurtosis of the main tumor voxels with SUV >τ.
int_SUVPeak_T_[τ]abs	Mean SUV of the main tumor voxels with SUV >τ in a spherical neighborhood of a radius of 8 voxels centered at the voxel with maximum SUV.
int_MTV_T_[τ]abs	Volume (in mm) of the ROI containing the main tumor voxels with SUV >τ.
int_TLG_T_[τ]abs	Total lesion glycosis of the ROI containing the main tumor voxels with SUV >τ.
int_SUVMean_T_[τ]rel	Mean SUV of the main tumor voxels with SUV >τ % of SUVMax.
int_SUVVariance_T_[τ]rel	SUV variance of the main tumor voxels with SUV >τ % of SUVMax.
int_SUVSkewness_T_[τ]rel	SUV skewness of the main tumor voxels with SUV >τ % of SUVMax.
int_SUVKurtosis_T_[τ]rel	SUV kurtosis of the main tumor voxels with SUV >τ % of SUVMax.
int_SUVPeak_T_[τ]rel	Mean SUV of the main tumor voxels with SUV >τ % of SUVMax in a spherical neighborhood of a radius of 8 voxels centered at the voxel with maximum SUV.
int_MTV_T_[τ]rel	Volume (in mm) of the ROI containing the main tumor voxels with SUV >τ % of SUVMax.
int_TLG_T_[τ]rel	Total lesion glycosis of the ROI containing the main tumor voxels with SUV >τ % of SUVMax.

Table .6: Feature-codes for intensity features used in the CSV file (part II): features extracted in ROI GTV_N

Feature-code	**Description**
int_SUVMean_N_[τ]abs	Mean SUV of the metastases voxels with SUV >τ.
int_SUVVariance_N_[τ]abs	SUV variance of the metastases voxels with SUV >τ.
int_SUVSkewness_N_[τ]abs	SUV skewness of the metastases voxels with SUV >τ.
int_SUVKurtosis_N_[τ]abs	SUV kurtosis of the metastases voxels with SUV >τ.
int_MTV_N_[τ]abs	Volume (in mm) of the ROI containing the metastases voxels with SUV >τ.
int_TLG_N_[τ]abs	Total lesion glycosis of the ROI containing the metastases voxels with SUV >τ.
int_SUVMean_N_[τ]rel	Mean SUV of the metastases voxels with SUV >τ % of SUVMax.
int_SUVVariance_N_[τ]rel	SUV variance of the metastases voxels with SUV >τ % of SUVMax.
int_SUVSkewness_N_[τ]rel	SUV skewness of the metastases voxels with SUV >τ % of SUVMax.
int_SUVKurtosis_N_[τ]rel	SUV kurtosis of the metastases voxels with SUV >τ % of SUVMax.
int_MTV_N_[τ]rel	Volume (in mm) of the ROI containing the metastases voxels with SUV >τ % of SUVMax.
int_TLG_N_[τ]rel	Total lesion glycosis of the ROI containing the metastases voxels with SUV >τ % of SUVMax.

Table .7: Feature-codes for distance features used in the CSV file.

Feature-code	**Description**
dst_TBarycenterN	Distance between barycenter of the main tumor and the barycenter of all metastases (see Eq. 12.10).
dst_sumDistTN	Cumulative distance between the barycenter of each metastasis and the barycenter of the main tumor (see Eq. 12.11).
dst_MTVweightedSumDistTN	MTV-weighted cumulative distance between the barycenter of each metastasis and the barycenter of the main tumor (see Eq. 12.12).
dst_maxDistTN	Maximum metastasis remoteness (see Eq. 12.13).
dst_MTVweightedMaxDistTN	MTV-weighted maximum metastasis remoteness (see Eq. 12.14).
dst_sumDistNBarycenterN	Cumulative distance between the barycenter of each metastasis and the barycenter of all metastases (see Eq. 12.15).
dst_MTVweightedSumDistNBarycenterN	MTV-weighted cumulative distance between the barycenter of each metastasis and the barycenter of all metastases (see Eq. 12.16).

Table .8: Feature-codes for texture features used in the CSV file.

Feature-code	**Description**
tex_GLCMsContrast_{*CT*,*PET*}_[*d*]_[*n*]	Contrast measure of the GLCMs computed with distance *d* and number of gray levels *n* for *CT* or *PET*.
tex_GLCMsCorrelation_{*CT*,*PET*}_[*d*]_[*n*]	Correlation measure of the GLCMs computed with distance *d* and number of gray levels *n* for *CT* or *PET*.
tex_GLCMsEnergy_{*CT*,*PET*}_[*d*]_[*n*]	Energy measure of the GLCMs computed with distance *d* and number of gray levels *n* for *CT* or *PET*.
tex_GLCMsHomogeneity_{*CT*,*PET*}_[*d*]_[*n*]	Homogeneity measure of the GLCMs computed with distance *d* and number of gray levels *n* for *CT* or *PET*.
tex_GLCMsEntropy_{*CT*,*PET*}_[*d*]_[*n*]	Entropy measure of the GLCMs computed with distance *d* and number of gray levels *n* for *CT* or *PET*.
tex_GLCMsInverseDiffMoment_{*CT*,*PET*}_[*d*]_[*n*]	Inverse difference moment measure of the GLCMs computed with distance *d* and number of gray levels *n* for *CT* or *PET*.
tex_GLCMsSumAverage_{*CT*,*PET*}_[*d*]_[*n*]	Sum average measure of the GLCMs computed with distance *d* and number of gray levels *n* for *CT* or *PET*.
tex_GLCMsSumEntropy_{*CT*,*PET*}_[*d*]_[*n*]	Sum entropy measure of the GLCMs computed with distance *d* and number of gray levels *n* for *CT* or *PET*.
tex_GLCMsSumVariance_{*CT*,*PET*}_[*d*]_[*n*]	Sum variance measure of the GLCMs computed with distance *d* and number of gray levels *n* for *CT* or *PET*.
tex_GLCMsDiffVariance_{*CT*,*PET*}_[*d*]_[*n*]	Difference variance measure of the GLCMs computed with distance *d* and number of gray levels *n* for *CT* or *PET*.
tex_GLCMsDiffEntropy_{*CT*,*PET*}_[*d*]_[*n*]	Difference entropy measure of the GLCMs computed with distance *d* and number of gray levels *n* for *CT* or *PET*.
tex_InnerLoG_{*CT*,*PET*}_sigma[σ]	LoG in the core of the main tumor with sigma σ for *CT* or *PET*.
tex_MarginLoG_{*CT*,*PET*}_sigma[σ]	LoG in the margin of the main tumor with sigma σ for *CT* or *PET*.
tex_InnerRieszN[*n*]_{*CT*,*PET*}_[*charDir*]_scale[*s*]	Riesz energy of the Riesz filter with direction *charDir* of order *n* and scale *s* in the core of the main tumor for *CT* or *PET*.
tex_MarginRieszN[*n*]_{*CT*,*PET*}_[*charDir*]_scale[*s*]	Riesz energy of the Riesz filter with direction *charDir* of order *n* and scale *s* in the margin of the main tumor for *CT* or *PET*.

Daniel Golden, and Daniel L. Rubin. Predicting treatment response in triple negative breast cancer from quantitative image analysis in perfusion MRI. *Medical Physics*, submitted.

6. Jocelyn Barker, Assaf Hoogi, Adrien Depeursinge, and Daniel L. Rubin. Automated classification of brain tumor type in whole-slide digital pathology images using local representative tiles. *Medical Image Analysis*, 30:60–71, 2016.
7. S. Basu, L. O. Hall, D. B. Goldgof, Yuhua Gu, V. Kumar, Jung Choi, R. J. Gillies, and R. A. Gatenby. Developing a classifier model for lung tumors in CT-scan images. In *IEEE International Conference on Systems, Man, and Cybernetics*, pages 1306–1312, October 2011.
8. Joel Castelli, B De Bari, Adrien Depeursinge, A Simon, A Devilliers, G Roman Jimenez, John Prior, R De Crevoisier, and J Bourhis. Overview of the predictive value of quantitative 18 FDG PET in head and neck cancer treated with chemoradiotherapy. *Critical Reviews in Oncology/Hematology*, 108:40–51, 2016.
9. Joel Castelli, Adrien Depeursinge, B. De Bari, Anne Devillers, R. De Crevoisier, J. Bourhis, and John O. Prior. Metabolic tumor volume and total lesion glycolysis in oropharyngeal cancer treated

with definitive radiotherapy: Which threshold is the best predictor of local control ? *Clinical Nuclear Medicine*, 2017.

10. Joel Castelli, Adrien Depeursinge, Vanessa Ndoh, John Prior, Esat Ozsahin, Anne Devillers, Hanan Bouchaab, Enrique Chajon, R. De Crevoisier, Nathaniel Scher, F. Jegoux, B. Laguerre, B. De Bari, and J. Bourhis. Development and validation of a PET-based nomogram predictive for survival of oropharyngeal cancer patients. *European Journal of Cancer*, 75:222–230, 2017.
11. Weijie Chen, Maryellen L Giger, Hui Li, Ulrich Bick, and Gillian M Newstead. Volumetric texture analysis of breast lesions on contrast–enhanced magnetic resonance images. *Magnetic Resonance in Medicine*, 58(3):562–571, sep 2007.
12. Nicolas Chenouard and Michael Unser. {3D} Steerable Wavelets in Practice. *IEEE Transactions on Image Processing*, 21(11):4522–4533, 2012.
13. Pol Cirujeda, Yashin Dicente Cid, Henning Müller, Daniel Rubin, Todd A Aguilera, Billy W Loo Jr., Maximilian Diehn, Xavier Binefa, and Adrien Depeursinge. A 3–D Riesz–Covariance Texture Model for Prediction of Nodule Recurrence in Lung CT. *IEEE Transactions on Medical Imaging*, 2016.
14. David A Clausi. An analysis of co-occurrence texture statistics as a function of grey level quantization. *Canadian Journal of remote sensing*, 28(1):45–62, 2002.
15. Adrien Depeursinge, Antonio Foncubierta-Rodríguez, Dimitri Van De Ville, and Henning Müller. Multiscale lung texture signature learning using the Riesz transform. In *Medical Image Computing and Computer–Assisted Intervention MICCAI 2012*, volume 7512 of *Lecture Notes in Computer Science*, pages 517–524. Springer Berlin / Heidelberg, October 2012.
16. Adrien Depeursinge, Antonio Foncubierta-Rodríguez, Dimitri Van De Ville, and Henning Müller. Three-dimensional solid texture analysis and retrieval in biomedical imaging: review and opportunities. *Medical Image Analysis*, 18(1):176–196, 2014.
17. Adrien Depeursinge, Camille Kurtz, Christopher F Beaulieu, Sandy Napel, and Daniel L Rubin. Predicting visual semantic descriptive terms from radiological image data: Preliminary results with liver lesions in CT. *IEEE Transactions on Medical Imaging*, 33(8):1–8, August 2014.
18. Adrien Depeursinge, Pedram Pad, Anne C Chin, Ann N Leung, Daniel L Rubin, Henning Müller, and Michael Unser. Optimized steerable wavelets for texture analysis of lung tissue in 3-D CT: classification of usual interstitial pneumonia. In *IEEE 12th International Symposium on Biomedical Imaging*, ISBI 2015, pages 403–406. IEEE, apr 2015.
19. Adrien Depeursinge, Masahiro Yanagawa, Ann N Leung, and Daniel L Rubin. Predicting Adenocarcinoma Recurrence Using Computational Texture Models of Nodule Components in Lung CT. *Medical Physics*, 42:2054–2063, 2015.
20. Yashin Dicente Cid, Henning Müller, Alexandra Platon, Pierre-Alexandre Poletti, and Adrien Depeursinge. Locally-Oriented Wavelet Transforms for 3-D Solid Texture Classification. *IEEE Transactions on Image Processing*, submitted.
21. Yu-Hua Dean Fang, Chien-Yu Lin, Meng-Jung Shih, Hung-Ming Wang, Tsung-Ying Ho, Chun-Ta Liao, and Tzu-Chen Yen. Development and Evaluation of an Open-Source Software Package CGITA for Quantifying Tumor Heterogeneity with Molecular Images. *BioMed Research International*, 2014, March 2014.
22. David V. Fried, Osama Mawlawi, Lifei Zhang, Xenia Fave, Shouhao Zhou, Geoffrey Ibbott, Zhongxing Liao, and Laurence E. Court. Potential use of 18f-fluorodeoxyglucose positron emission tomography-based quantitative imaging features for guiding dose escalation in stage III non-small cell lung cancer. *International Journal of Radiation Oncology*Biology*Physics*, 94(2):368–376, 2016.
23. David V. Fried, Osama Mawlawi, Lifei Zhang, Xenia Fave, Shouhao Zhou, Geoffrey Ibbott, Zhongxing Liao, and Laurence E. Court. Stage III non-small cell lung cancer: Prognostic value of FDG PET quantitative imaging features combined with clinical prognostic factors. *Radiology*, 278(1):214–222, 2016.
24. B. Ganeshan, K. Skogen, I. Pressney, D. Coutroubis, and K. Miles. Tumour heterogeneity in oesophageal cancer assessed by CT texture analysis: Preliminary evidence of an association with tumour metabolism, stage, and survival. *Clinical Radiology*, 67(2):157–164, 2012.

25. Balaji Ganeshan, Sandra Abaleke, Rupert C D Young, Christopher R Chatwin, and Kenneth A Miles. Texture analysis of non–small cell lung cancer on unenhanced computed tomography: initial evidence for a relationship with tumour glucose metabolism and stage. *Cancer Imaging*, 10:137–143, jul 2010.
26. Balaji Ganeshan, Vicky Goh, Henry C. Mandeville, Quan Sing Ng, Peter J. Hoskin, and Kenneth A. Miles. Non-small cell lung cancer: Histopathologic correlates for texture parameters at CT. *Radiology*, 266(1):326–336, 2013.
27. Balaji Ganeshan, Elleny Panayiotou, Kate Burnand, Sabina Dizdarevic, and Kenneth A. Miles. Tumour heterogeneity in non-small cell lung carcinoma assessed by CT texture analysis: a potential marker of survival. *European Radiology*, 22(4):796–802, 2012.
28. Robert A Gatenby, Olya Grove, and Robert J Gillies. Quantitative Imaging in Cancer Evolution and Ecology. *Radiology*, 269(1):8–14, 2013.
29. Pantelis Georgiadis, Dionisis Cavouras, Ioannis Kalatzis, Dimitris Glotsos, Emmanouil Athanasiadis, Spiros Kostopoulos, Koralia Sifaki, Menelaos Malamas, George Nikiforidis, and Ekaterini Solomou. Enhancing the discrimination accuracy between metastases, gliomas and meningiomas on brain MRI by volumetric textural features and ensemble pattern recognition methods. *Magnetic Resonance Imaging*, 27(1):120–130, January 2009.
30. Marco Gerlinger, Andrew J Rowan, Stuart Horswell, James Larkin, David Endesfelder, Eva Gronroos, Pierre Martinez, Nicholas Matthews, Aengus Stewart, Patrick Tarpey, Ignacio Varela, Benjamin Phillimore, Sharmin Begum, Neil Q McDonald, Adam Butler, David Jones, Keiran Raine, Calli Latimer, Claudio R Santos, Mahrokh Nohadani, Aron C Eklund, Bradley Spencer-Dene, Graham Clark, Lisa Pickering, Gordon Stamp, Martin Gore, Zoltan Szallasi, Julian Downward, P Andrew Futreal, and Charles Swanton. Intratumor Heterogeneity and Branched Evolution Revealed by Multiregion Sequencing. *New England Journal of Medicine*, 366(10):883–892, 2012.
31. Olivier Gevaert, Lex A Mitchell, Achal S Achrol, Jiajing Xu, Sebastian Echegaray, Gary K Steinberg, Samuel H Cheshier, Sandy Napel, Greg Zaharchuk, and Sylvia K Plevritis. Glioblastoma Multiforme: Exploratory Radiogenomic Analysis by Using Quantitative Image Features. *Radiology*, 273(1):168–174, 2014.
32. Olivier Gevaert, Jiajing Xu, Chuong D Hoang, Ann N Leung, Yue Xu, Andrew Quon, Daniel L Rubin, Sandy Napel, and Sylvia K Plevritis. Non–Small Cell Lung Cancer: Identifying Prognostic Imaging Biomarkers by Leveraging Public Gene Expression Microarray Data — Methods and Preliminary Results. *Radiology*, 264(2):387–396, 2012.
33. Robert M Haralick. Statistical and Structural Approaches to Texture. *Proceedings of the IEEE*, 67(5):786–804, may 1979.
34. Robert M. Haralick, K. Shanmugam, and Its'hak Dinstein. Textural features for image classification. *IEEE Transactions on Systems, Man and Cybernetics*, 3(6):610–621, November 1973.
35. André Huisman, Lennert S. Ploeger, Hub F. J. Dullens, Trudy N. Jonges, Jeroen A. M. Belien, Gerrit A Meijer, Neal Poulin, William E Grizzle, and Paul J. van Diest. Discrimination between benign and malignant prostate tissue using chromatin texture analysis in 3D by confocal laser scanning microscopy. *The Prostate*, 67(3):248–254, February 2007.
36. C Carl Jaffe. Imaging and Genomics: is there a synergy? *Radiology*, 264(2):329–331, 2012.
37. Tae Yun Kim, H J Choi, H Hwang, and Heung Kook Choi. Three–dimensional Texture Analysis of Renal Cell Carcinoma Cell Nuclei for Computerized Automatic Grading. *Journal of Medical Systems*, 34(4):709–716, aug 2010.
38. Tae Yun Kim and Heung Kook Choi. Computerized Renal Cell Carcinoma Nuclear Grading Using {3D} Textural Features. In *IEEE International Conference on Communications Workshops, 2009. ICC Workshops 2009.*, pages 1–5, jun 2009.
39. Despina Kontos, Predrag R Bakic, Ann-Katherine Carton, Andrea B Troxel, Emily F Conant, and Andrew D A Maidment. Parenchymal Texture Analysis in Digital Breast Tomosynthesis for Breast Cancer Risk Estimation: A Preliminary Study. *Academic Radiology*, 16(3):283–298, 2009.
40. Virendra Kumar, Yuhua Gu, Satrajit Basu, Anders Berglund, Steven A. Eschrich, Matthew B. Schabath, Kenneth Forster, Hugo J. W. L. Aerts, Andre Dekker, David Fenstermacher, Dmitry B. Goldgof, Lawrence O. Hall, Philippe Lambin, Yoganand Balagurunathan, Robert A. Gatenby, and Robert J. Gillies. Radiomics: the process and the challenges. *Magnetic Resonance Imaging*, 30(9):1234–1248, 2012.

41. Ralph T H Leijenaar, Georgi Nalbantov, Sara Carvalho, Wouter J C van Elmpt, Esther G C Troost, Ronald Boellaard, Hugo J W L Aerts, Robert J Gillies, and Philippe Lambin. The effect of SUV discretization in quantitative FDG-PET Radiomics: the need for standardized methodology in tumor texture analysis. *Scientific Reports*, 5:11075, August 2015.
42. Anant Madabhushi, Michael D. Feldman, Dimitris N. Metaxas, Deborah Chute, and John E. Tomaszeweski. A novel stochastic combination of 3D texture features for automated segmentation of prostatic adenocarcinoma from high resolution MRI. In *Medical Image Computing and Computer-Assisted Intervention - MICCAI 2003, 6th International Conference*, pages 581–591, November 2003.
43. Doaa Mahmoud-Ghoneim, Grégoire Toussaint, Jean-Marc Constans, and Jacques D. de Certaines. Three dimensional texture analysis in MRI: a preliminary evaluation in gliomas. *Magnetic Resonance Imaging*, 21(9):983–987, November 2003.
44. Sarah A. Mattonen, David A. Palma, Cornelis J. A. Haasbeek, Suresh Senan, and Aaron D. Ward. Early prediction of tumor recurrence based on CT texture changes after stereotactic ablative radiotherapy (SABR) for lung cancer. *Medical Physics*, 41(3):1–14, 2014.
45. Nicolas Michoux, Laurent Bollondi, Adrien Depeursinge, Latifa Fellah, Isabelle Leconte, and Henning Müller. Is tumor heterogeneity quantified by 3D texture analysis of MRI able to predict non-response to NAC in breast cancer? In *European Society for Magnetic Resonance in Medicine and Biology*, ESMRMB, 2016.
46. Nicolas Michoux, Laurent Bollondi, Adrien Depeursinge, Antoine Geissbuhler, Latifa Fellah, Henning Müller, and Isabelle Leconte. Predicting non-response to NAC in patients with breast cancer using 3D texture analysis. In *European Congress of Radiology (ECR2015)*, ECR2015, Vienna, Autria, mar 2015.
47. Reza Mirnezami, Jeremy Nicholson, and Ara Darzi. Preparing for Precision Medicine. *New England Journal of Medicine*, 366(6):489–491, 2012.
48. Sandy Napel and Maryellen Giger. Special Section Guest Editorial:Radiomics and Imaging Genomics: Quantitative Imaging for Precision Medicine. *Journal of Medical Imaging*, 2(4):41001, 2015.
49. G. De Nunzio, G. Pastore, M. Donativi, A. Castellano, and A. Falini. A CAD system for cerebral glioma based on texture features in DT-MR images. *Nuclear Instruments and Methods in Physics Research Section A: Accelerators, Spectrometers, Detectors and Associated Equipment*, 648, Suppl(0):100–102, 2011.
50. Fanny Orlhac, Michaël Soussan, Jacques-Antoine Maisonobe, Camilo A Garcia, Bruno Vanderlinden, and Irène Buvat. Tumor Texture Analysis in 18F-FDG PET: Relationships Between Texture Parameters, Histogram Indices, Standardized Uptake Values, Metabolic Volumes, and Total Lesion Glycolysis. *Journal of Nuclear Medicine*, 55(3):414–422, 2014.
51. Sebastian Otálora, Angel Cruz Roa, John Arevalo, Manfredo Atzori, Anant Madabhushi, Alexander Judkins, Fabio González, Henning Müller, and Adrien Depeursinge. Combining Unsupervised Feature Learning and Riesz Wavelets for Histopathology Image Representation: Application to Identifying Anaplastic Medulloblastoma. In Nassir Navab, Joachim Hornegger, William M Wells, and Alejandro Frangi, editors, *Medical Image Computing and Computer-Assisted Intervention — MICCAI 2015*, volume 9349 of *Lecture Notes in Computer Science*, pages 581–588. Springer International Publishing, oct 2015.
52. Marco Ravanelli, Davide Farina, Mauro Morassi, Elisa Roca, Giuseppe Cavalleri, Gianfranco Tassi, and Roberto Maroldi. Texture analysis of advanced non-small cell lung cancer (NSCLC) on contrast-enhanced computed tomography: prediction of the response to the first-line chemotherapy. *European Radiology*, 23(12):3450–3455, 2013.
53. L K Soh and C Tsatsoulis. Texture analysis of SAR sea ice imagery using gray level co-occurrence matrices. *IEEE Transactions on Geoscience and Remote Sensing*, 37(2):780–795, mar 1999.
54. Geoffrey Sonn, Lewis D. Hahn, Richard Fan, Jocelyn Barker, Adrien Depeursinge, and Daniel L. Rubin. Quantitative image texture analysis predicts malignancy on multiparametric prostate MRI. In *91st Annual Meeting of the Western Section of American Urological Association*, WSAUA, October 2015.
55. J P Ward, P Pad, and M Unser. Optimal Isotropic Wavelets for Localized Tight Frame Representa-

tions. *IEEE Signal Processing Letters*, 22(11):1918–1921, nov 2015.